Processes of Colliding Cold Pools Derived from a 356-m-High Shenzhen Met-Tower during an Extremely Heavy Rainfall Event

CHUYING MAI,[a,b] YU DU,[a,c,d] AND MINGHUA LI[e]

[a] *School of Atmospheric Sciences, Sun Yat-sen University, and Southern Marine Science and Engineering Guangdong Laboratory (Zhuhai), Zhuhai, China*
[b] *Key Laboratory of South China Sea Meteorological Disaster Prevention and Mitigation of Hainan Province, China Meteorological Administration, Haikou, China*
[c] *Guangdong Province Key Laboratory for Climate Change and Natural Disaster Studies, Sun Yat-sen University, Guangzhou, China*
[d] *Key Laboratory of Tropical Atmosphere-Ocean System, Sun Yat-sen University, Ministry of Education, Guangzhou, China*
[e] *Meteorological Bureau of Shenzhen Municipality, and Key Laboratory of Severe Weather in South China, Shenzhen, China*

(Manuscript received 4 August 2022, in final form 2 March 2023, accepted 3 March 2023)

ABSTRACT: Convectively generated cold pools play a crucial role in the convection initiation and development, but observations of their vertical structure are insufficient. In this study, quantitative vertical evolutions of cold pools during a high-impact heavy rainfall event near the south coast of China were examined using observations from a 356-m-high Shenzhen Met-Tower, and their potential impacts on heavy rainfall were further discussed through high-resolution surface station network and radar observations. On 11 April 2019, heavy precipitation occurred near metropolitan Shenzhen, lasting for 50 min at its southern downtown and resulting in 11 deaths. During this event, a shallow cold pool was first observed by the tower and yielded a long-lasting cooling of 2.6 K. Approximately 1 h later, another deeper cold pool accompanied by a squall line was added from the west. This addition resulted in a more abrupt and intense surface temperature deficit (5.1 K) and stronger gusty winds (23 m s^{-1}). When the two cold pools collided near Shenzhen, the low-level winds converged at their intersection, dynamically enhancing the heavy-rain-producing squall line. Moreover, the collision of the two cold pools reduced the temperature gradient at the northern edge of the merged cold pool, which could inhibit development of the squall line. The area south of the squall line became a relatively favorable environment for convection initiation, given the warm and moist oceanic environment. Consequently, the squall line turned northeast–southwest, forming a training line mode that was nearly parallel to the eastward movement. This training line mode prolonged the precipitation duration in the southern downtown area.

KEYWORDS: Convective storms/systems; Boundary layer; Cold pools

1. Introduction

Since rainfall evaporation into the subcloud layer latently cools the downdraft air, the cooled air reaches the surface and generates horizontally spread density currents, which are called cold pools (Zipser 1977). Cold pools significantly affect convection initiation and development, and subsequently influence the formation and maintenance of heavy rainfall (e.g., Du et al. 2020b; Wang et al. 2014; Jeong et al. 2016; Peters and Schumacher 2015; Tsuguti and Kato 2014).

Both the dynamic and thermodynamic properties of cold pools can create a preferred region for secondary convection initiation (Torri et al. 2015). Dynamically, the interplay between horizontal vorticity generated by the buoyancy gradient at the head of cold pools and vorticity from the background vertical wind shear results in lifting of the outside less dense warm air parcels, which is classical mechanical lifting theory for the organization of convective systems such as squall lines (RKW theory, e.g., Rotunno et al. 1988; Weisman et al. 1988; Weisman and Rotunno 2004; Bryan and Rotunno 2014). Cold pools interacting with low-level background winds can also provide mechanical lifting even in the absence of wind shear (Torri et al. 2015; Goff 1976). When two cold pools collide, lifting becomes stronger (Feng et al. 2015; Haerter 2019; Purdom 1976; Weaver and Nelson 1982; Torri and Kuang 2019; Meyer and Haerter 2020). From a thermodynamic perspective, tropical cold pools are identified with enhanced near-surface moisture at their leading edge, called moisture rings. This structure promotes triggering of new convection with enhanced moist static energy even in low-wind-shear conditions (Tompkins 2001; Torri and Kuang 2016). However, moisture rings and their influence are usually found in numerical simulations and are seldom observed (de Szoeke et al. 2017; Chandra et al. 2018). These effects of cold pools on convection initiation and organization, which depend on their own properties, need further observational evidence to verify the mechanisms found by numerical studies.

Heavy rainfall is usually associated with mesoscale convective systems (MCSs) in two organizational modes: "back building or quasi-stationary" and "training line" (Maddox et al. 1979; Schumacher and Johnson 2005, 2006). Convective cells are repeatedly triggered upstream of the back-building MCS, and the MCS thus remains quasi-stationary. The training line predominantly moves parallel with the orientation of linear convection. The two organizational modes would both produce large accumulative rainfall over a particular area with the repeated passage of convective cells (Doswell et al. 1996).

Corresponding author: Yu Du, duyu7@mail.sysu.edu.cn

DOI: 10.1175/MWR-D-22-0214.1

MCSs in the two modes are often controlled by cold pool outflows (Peters and Schumacher 2015, 2016; Jeong et al. 2016; Wang et al. 2014). Near the coast of South China, several observational studies within the Southern China Monsoon Rainfall Experiment have documented that the outflows from cold pools in the moist environment lift highly unstable moist air from the ocean, resulting in continuous convection initiations along the mesoscale outflow boundary. The training convective cells and rainbands then form and move slowly through a particular region, causing long-lasting rainfall (Wang et al. 2014; Wu and Luo 2016; Liu et al. 2018). Liu et al. (2018) found that the intersection of upstream unstable oceanic air masses with cold pool outflows and strong rear inflows builds a rapid splitting and reestablishment process of bowing rainbands. This process eventually contributes to the formation of rainband training. Although the contributions of cold pool outflow to the production of heavy rainfall are revealed by a few studies (Tsuguti and Kato 2014; Liu et al. 2018), more observational studies are still needed to focus on the detailed evolution processes of cold pools and their possible roles in the formation of heavy rainfall.

Rapid variations in near-surface properties of cold pools can be observed by the high temporal resolution of surface measurements in various environmental conditions, such as surface meteorological sites (e.g., Engerer et al. 2008; Chandra et al. 2018) and mobile mesonets (e.g., Geerts et al. 2017; Miller et al. 2020) on land, and uncrewed surface vehicles and moored buoys over oceans (e.g., Wills et al. 2021; Feng et al. 2015; Joseph et al. 2021). For instance, cold pools over the equatorial Indian Ocean are documented with an average temperature decrease of ~1.5 K, a decrease in the water vapor mixing ratio of ~1 g kg^{-1} and wind speed increase of 2 m s^{-1} (Chandra et al. 2018). Stronger signals of cold pool passage are found over midlatitude continents than over tropical oceans (e.g., Joseph et al. 2021; Kirsch et al. 2021; Engerer et al. 2008). Passages of cold pools in the midlatitude continent at Oklahoma can cause potential temperature anomalies between 5.4 and 11 K, a pressure increase between 3.2 and 4.5 hPa, and gusty winds larger than 15 m s^{-1} (Engerer et al. 2008).

Vertical structures of cold pools are insufficiently understood due to a lack of vertical observations, for example, their depth and strength, which are important parameters in the process of triggering new convective cells (Borque et al. 2020; Engerer et al. 2008; Rotunno et al. 1988). Although some laboratory experiments and idealized numerical simulations have presented the structure of density current, the observational evidence remains insufficient, and vertical distributions of parameters in and above cold pools are poorly observed (Zuidema et al. 2017). Vertical observational characteristics of cold pools are also needed for guidance and physical constraints for better parameterization, which would help to generate improved reproduction of the environment and a more realistic diurnal cycle of precipitation in climate or regional weather models (Del Genio et al. 2012; Maloney and Hartmann 2001; Rio et al. 2009; Schlemmer and Hohenegger 2014; Hirt and Craig 2021; Schiro and Neelin 2018; Chandra et al. 2018). From radar analysis of a case in Oklahoma, the cold pool leading edge was estimated with large spatial and temporal variations in its height but a constant propagation speed (Borque et al. 2020). Using radiosonde data, Hitchcock et al. (2019) estimated the strengths and depths of cold pools associated with nocturnal MCSs during the Plains Elevated Convection at Night field campaign. van den Heever et al. (2021) used a number of novel campaign strategies, including radiosonde, and found that cold pools in the continental United States obtain a range of depths from 200 to 2300 m and have a variety of vertical temperature structures. Using the tower measure, cold pool depths are estimated to be ~500 m on average in the Netherlands (Kruse et al. 2022) and 746 m in Hamburg, Germany (Kirsch et al. 2021), both of which are higher than the typical cold pool height over the ocean (e.g., ~300 m; Terai and Wood 2013). Kruse et al. (2022) further revealed the vertical circulation, vertical stratification in temperature and moisture anomalies at different portions of the cold pool.

However, observational studies of cold pools are still missing in some regions (e.g., South China) where the influences of cold pools are also significant. The coastal South China region frequently encounters the convergence of moist tropical oceanic airflows with drier midlatitude continental flows. Since cold pools are significantly influenced by environmental moisture, it is necessary to study their characteristics in this specific region where the moisture conditions are different from those in the tropical and midlatitude regions. Shenzhen Met-Tower is located in coastal South China. It is 356 m high and is equipped with a high vertical resolution with 13 measurement levels. The Met-Tower is the second highest mast structure in the world and the highest in Asia (Sun et al. 2020). It has been widely used to measure vertical meteorological and environmental parameters (Li et al. 2020; Chen et al. 2020; Sun et al. 2020). It provides a good opportunity to detect temporal and vertical variations in the boundary layer from the surface to the urban canopy during passages of cold pools in coastal South China.

On 11 April 2019, an extremely heavy rainfall event occurred in Shenzhen city, South China (Fig. 1). This event resulted in a maximum 30-min precipitation of 73.4 mm, which breaks the historical high during April; this event was also responsible for 11 fatalities. In the present study, the vertical features of cold pools during the heavy rainfall event are investigated with the help of the Shenzhen Met-Tower. The present study aims to achieve the following objectives: 1) to examine the fine spatiotemporal evolution of cold pool properties from both vertical and horizontal perspectives and 2) to explore the possible impacts of cold pools on the development of convection and the precipitation process from a purely observational perspective. The remainder of this paper is organized as follows: section 2 introduces the observational measurements and data used. Section 3 presents an overview of the precipitation process and detailed background conditions during the heavy rainfall event. Vertical variations in cold pool properties detected by the Shenzhen Met-Tower are described in section 4. Section 5 discusses the temporal evolution and the roles of cold pools in heavy rainfall. A summary and discussion are shown in the final section 6.

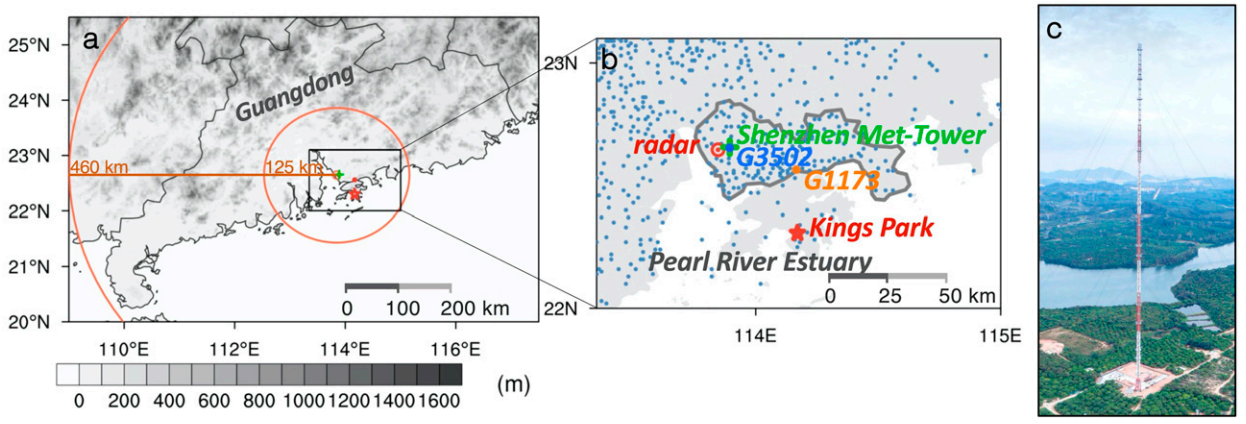

FIG. 1. (a),(b) Locations of observation sites in Guangdong Province. The gray shading in (a) indicates terrain height (m). The box denotes the enlarged domain shown in (b). The orange circles with radii of 125 and 460 km represent the PPI scanning range at highest elevation and the maximum detection range of Shenzhen radar at lowest elevation, respectively. (b) The gray outline represents the range of Shenzhen city. The small blue dots denote the locations of in situ surface stations near the area of interest. The large blue and orange dots represent the locations of Stations G3502 and G1173, respectively. The green cross, red circle, and red star denote the locations of the Shenzhen Met-Tower, Shenzhen radar, and Kings Park sounding station, respectively. (c) Photograph of the Shenzhen Met-Tower.

2. Observational data

Figures 1a and 1b show the locations of multiple observation platforms used in this study to describe the heavy rainfall event and the associated three-dimensional features of cold pools that occurred on 11 April 2019, in Shenzhen city.

The 356-m-high Shenzhen Met-Tower (Fig. 1c) is located in Shenzhen city (22.66°N, 113.89°E), denoted as a green cross in Figs. 1a and 1b. The Met-Tower is equipped with instruments for basic meteorological observations, detecting meteorological variables including temperature, horizontal wind speed and direction, and relative humidity at 13 platforms (10, 20, 40, 50, 80, 100, 150, 160, 200, 250, 300, 320, and 350 m), and pressure at 3 layers (50, 100, and 300 m). These variables are available at a temporal resolution of 10 s to assess the detailed evolution of cold pools. To correct for the overestimation of relative humidity by sensors in nearly saturated conditions, bias correction was performed using long-term data from 2018 to 2020. The original relative humidity data were divided into two groups based on 10-m relative humidity that was lower or greater than 70%. Biases were calculated for each group by determining the difference between the group average of data during 2018–20 and the estimation value from a linear regression between the height and the group average at specific levels (10, 40, 50, 100, 150, 200, and 250 m), where relative humidity was not overestimated as oversaturation. Additionally, any relative humidity values over 100% were corrected to 100%. The specific humidity (q, kg kg^{-1}) is obtained based on the following equation:

$$q = \frac{0.622 e_s}{p - 0.378 e_s} \times \frac{\mathrm{rh}}{100},$$

where t, p, and rh are the temperature (°C), pressure (hPa), and relative humidity (%), respectively, derived from the Met-Tower, and the saturation vapor pressure e_s is calculated with the equations in Alduchov and Eskridge (1996) :

$$e_s = 1.000\,71 \times e^{0.000\,004\,5p} e_w$$

and

$$e_w = 6.1094 \times 10^{17.625t/(243.04+t)}.$$

To present the development of precipitation and surface features of cold pools, in situ surface observations of 5-min internals are used. In total, 2825 stations in Guangdong Province are used, but only the locations of stations near the area of interest are presented in Fig. 1b. The surface observations record 10-m wind values averaged within 2 min, instantaneous 1.5-m temperature and pressure, and 5-min precipitation accumulation. G3502 is an in situ surface weather station (blue dot in Fig. 1b) located ~250 m near the Shenzhen Met-Tower and acts as a supplement of precipitation observations for the tower data. The G1173 station (orange dot in Fig. 1b) is located in southern downtown Shenzhen, where rainfall peaked during the event.

The S-band Shenzhen Doppler radar (red circle in Fig. 1b) collects surveillance scans every 6 min. The radar has a range-gate spacing of 250 m and nine elevations from 0.5° to 19.5°. The orange circles in Fig. 1a show the scanning radius of approximately 125 km at the highest elevation and 460 km at the lowest elevation. The achieved radar base data are finally interpolated to a horizontal grid resolution of 0.05° × 0.05° using natural neighbor interpolation. After interpolation, the maximum reflectivity at the nine elevations is calculated as composite reflectivity. The vertical environmental stratification near Shenzhen city is revealed by the radiosonde sounding released every 12 h at Kings Park (red star in Fig. 1b). To show the synoptic background, reanalysis data from the National Centers for Environmental Prediction Final Operational

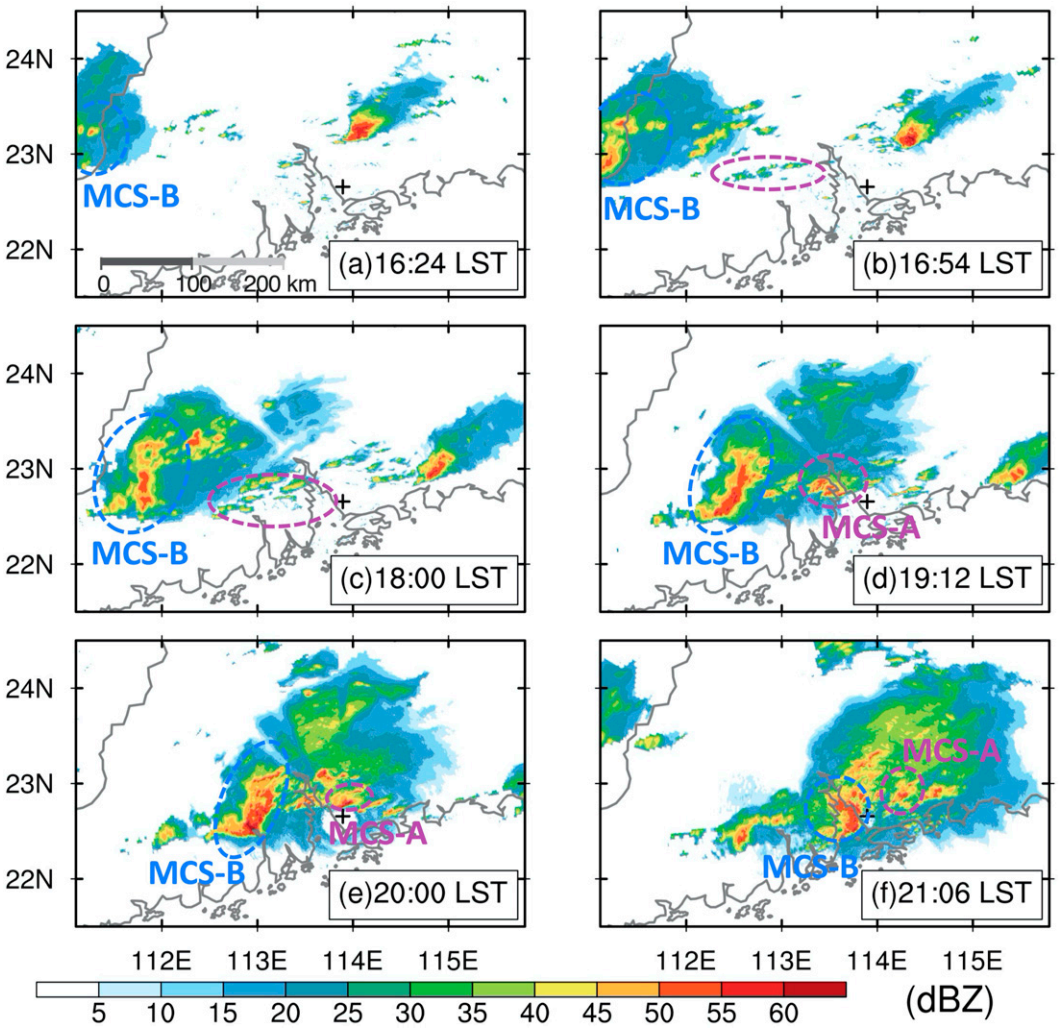

FIG. 2. Temporal evolution of composite reflectivity (dBZ) derived from Shenzhen radar at (a) 1624, (b) 1654, (c) 1800, (d) 1912, (e) 2000, and (f) 2106 LST 11 Apr 2019. The black cross denotes the location of Shenzhen Met-Tower. Purple and blue dashed ovals indicate the approximate locations of MCS-A and MCS-B, respectively.

Global Analysis (NCEP FNL) is adopted, which is available every 6 h with a spatial resolution of 0.25° × 0.25°.

3. Case overview

Figure 2 depicts the overall temporal evolution of MCSs within the heavy rainfall event. After entering the Guangdong Province from the west at 1600 local standard time (LST = UTC + 8 h), MCS-B moved eastward across the domain (Fig. 2a). During the eastward movement of MCS-B, a number of convective cells were initiated west of the Pearl River Estuary and then organized into MCS-A (purple oval in Figs. 2b–d). Then, MCS-A moved eastward and passed to the north of Shenzhen (Fig. 2e). Meanwhile, MCS-B gradually developed into a strong squall line characterized by a bow-shaped echo (Fig. 2e). At 2106 LST, the strengthened MCS-B approached Shenzhen Met-Tower and began to produce heavy precipitation over Shenzhen city (Fig. 2f). It is worthy to note that the MCS-B at the initial time was located beyond the PPI scanning range of 125 km at the highest elevation. However, the movement of the MCS out of the study domain and the detailed evolutions of the MCSs within the domain, can be displayed using the single Shenzhen radar due to the maximum detection radius of 460 km.

The squall line MCS-B produced severe convective weather in and around Shenzhen city, including short-duration heavy rainfall, strong winds, hail and 704 lightning strikes during 2025–2325 LST. The maximum instantaneous surface wind speed was recorded as 16.1 m s^{-1} south of Shenzhen city at 2155 LST. Violent and abrupt rainfall generated maximum 5-min precipitation more than 10 mm at 56.8% of the in situ stations of Shenzhen city and was even mostly concentrated in only 10 min (e.g., G3502 in Fig. 3a). Intense rainfall south of Shenzhen lasted longer, for example, at G1173 in Fig. 3a for nearly 50 min. G1173 recorded cumulative precipitation of 63 mm within only 30 min, which even equals the maximum

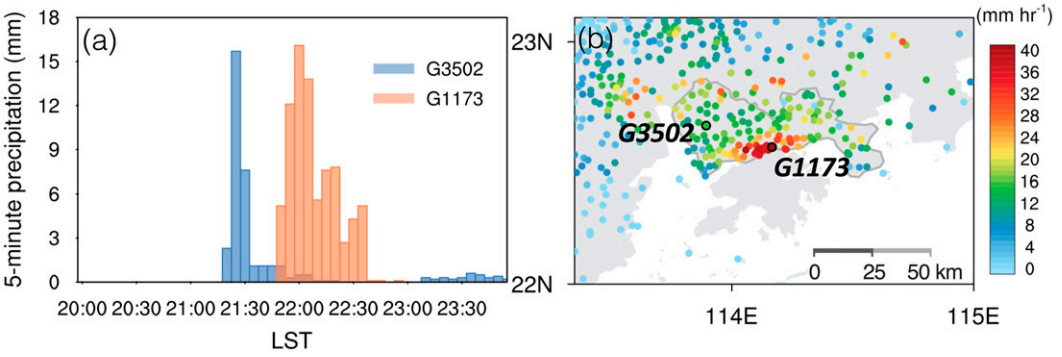

FIG. 3. (a) Time series of 5-min precipitation accumulation (mm) at G3502 (blue bars) and G1173 (orange bars) in situ surface stations. (b) Distribution of hourly precipitation (mm h^{-1}) averaged during 2100–2255 LST. The black circles represent the locations of stations G3502 and G1173.

10-h accumulated precipitation in another heavy rainfall event (Luo et al. 2020). The accumulated precipitation of 27 in situ stations in southern Shenzhen during 1200–2355 LST exceeded 50 mm, reaching the daily precipitation threshold of heavy rainfall according to the China Meteorological Administration. The prolonged intense rainfall produced heavier hourly precipitation of over 40 mm h^{-1} on average during 2100–2255 LST south of Shenzhen (Fig. 3b), which is the downtown area with the densest population, and caused 11 fatalities.

Synoptic background circulations at 1400 and 2000 LST 11 April are shown in Fig. 4 using the reanalysis data from NCEP FNL. At lower levels, the northwesterly flow with cold air north of Guangdong converged with the southwesterly flow transporting the oceanic warm and moist air, and thus, a west–east-oriented shear line was formed (Fig. 4a). Along the shear line, a long linear convergence zone at low levels favored the development and maintenance of MCSs (Fig. 4b), which is a typical synoptic pattern of heavy rainfall in South China (Chen et al. 2022). The shear line moved southward afterward, and the northeasterly winds to the north moved farther south as well (Figs. 4b,d).

As shown in Fig. 5, the skew T–log$p$ diagram of the radio sounding at Kings Park indicated a favorable thermodynamic environment for MCS development. The low-level environment

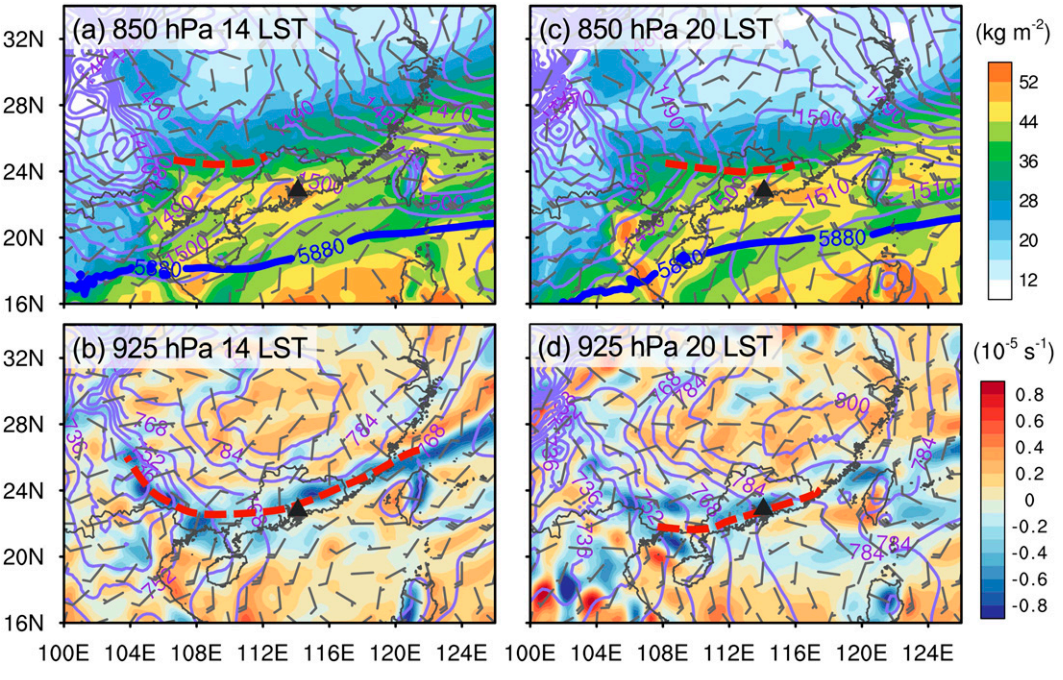

FIG. 4. Horizontal distributions of reanalysis geopotential height (gpm, contours) and wind vectors from NCEP FNL at (a),(c) 850 and (b),(d) 925 hPa at (left) 1400 and (right) 2000 LST 11 Apr 2019. The shading in (a) and (c) is precipitable water (kg m^{-2}), and that in (b) and (d) is divergence (10^{-5} s^{-1}) at 925 hPa. The thick blue lines in (a) and (c) denote the contour of 5880-gpm geopotential height at 500 hPa. The red thick dashed lines in (a)–(d) denote the shear lines. The triangles represent the location of Shenzhen city.

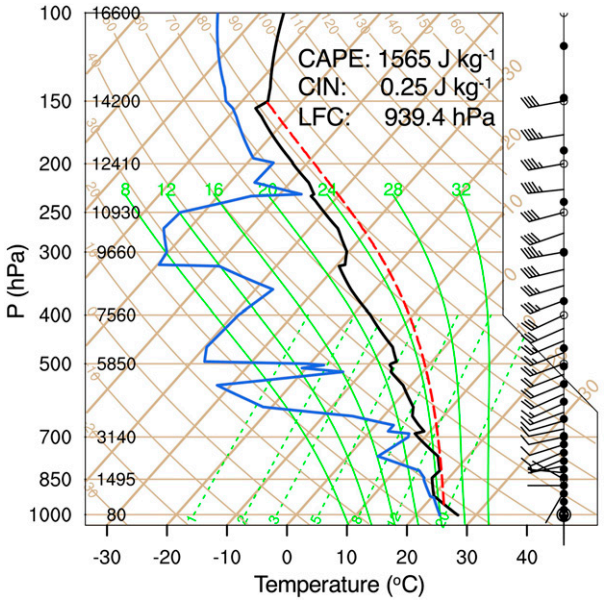

FIG. 5. Skew T–log$p$ diagram of the radio sounding at Kings Park (location denoted by red star in Fig. 1) at 2000 LST 11 Apr 2019. Surface-based CAPE (J kg^{-1}), CIN (J kg^{-1}), and LFC (hPa) are given in the top-right corner. The blue and black lines represent the vertical profiles of the dewpoint temperature and temperature, respectively. The red dashed line represents the parcel path.

was moist, especially nearly saturated at layers near 925 and 700 hPa. The moist low-level environment produced moderate convective available potential energy (CAPE, 1565 J kg^{-1}), negligible convective inhibition (CIN, 0.25 J kg^{-1}) and a low level of free convection (LFC, 939.4 hPa). Moderate CAPE was also contributed by the relatively cold air at middle levels. A dry layer occurred between 600 and 250 hPa above the low-level moist layer. The sounding revealed an estimated precipitable water of 47.70 mm. CAPE, CIN, LFC and precipitable water shows comparable magnitudes for other extreme rainfall events in coastal South China (Sun et al. 2021; Liu et al. 2018; Wang et al. 2014). Horizontal winds veered from southerly at near-surface to southwesterly at midlevel, with a vertical shear of ~23.15 m s^{-1} beneath the midlevel (500 hPa). The moderate vertical wind shear was conducive to the development of MCSs.

Therefore, the background environment was both dynamically and thermodynamically favorable for convection initiation and MCS maintenance, resulting in strongly convective heavy rainfall.

4. Characteristics of cold pools derived from Shenzhen Met-Tower

During heavy rainfall, Shenzhen Met-Tower captured the vertical evolution of the boundary layer structure and identified the passage of cold pools, as shown in Fig. 6. The Met-Tower observed two rapid temperature drops near 2008 and 2116 LST (Fig. 6a) as MCS-A and MCS-B passed by Shenzhen, respectively (Figs. 2e,f). Both temperature decreases also corresponded to pressure increases (Fig. 6c). The results suggest the passages of two cold pools associated with MCS-A and MCS-B at Shenzhen Met-Tower.

The passage of the cold pool from MCS-A caused the first temperature deficit of approximately 2.6 K in 8 min at all measurement levels (10–350 m) after 2008 LST (Fig. 6a). The temperature at 350 m recovered quickly with an increase of nearly 2.1 K in 11 min immediately after the 8-min decrease, but the temperature recovery was not evident at lower levels, with a minor increase of 0.4 K at 100 m. The temperature recovery was more rapid than the statistically average results in previous studies [e.g., 1 h 20 min in Joseph et al. (2021)]. The temperature at 300–350 m then decreased again with a smaller magnitude of 0.7 K. The decrease, increase and decrease fluctuations of temperature at the higher levels (150–350 m) suggested the passage of vertical bulge structures in the cold pool at the top of cold air masses instead of the recovery after cold pool passage. The first bulge is probably the "head" of the cold pool and can be seen in laboratory simulated density currents (e.g., Charba 1974). The temperature increase at high layers between the two cooling events was caused by warm air intrusion into the cold pool, which was probably related to Kelvin–Helmholtz instabilities or superimposed with lobe and cleft instabilities and can create turbulent mixing behind the cold pool head (Grant and van den Heever 2016; Meyer and Haerter 2020). At levels lower than 100 m, only slight warming was detected, which suggested the lasting influence of the body of the cold pool. The result suggests that the depth of the cold pool body behind the head was approximately equal to 100 m. After the smaller cooling, the temperature above 100 m gradually recovered, but the temperature was still lower than before 2008 LST, which can be attributed to nocturnal radiation cooling and the existence of stratiform precipitation.

At 2116 LST, with the passage of MCS-B, another more rapid temperature drop occurred with a larger magnitude (Fig. 6a). The magnitude of cooling at 10–100 m was approximately 5.1 K in 15 min. The cooling weakened with increasing height (e.g., 4 K deficit at 300 m). Due to the existence of stratiform precipitation behind (Fig. 2f), the low temperature in the boundary layer lasted for a longer time until nearly 40 min after cooling (2116–2156 LST). The long-lasting strong temperature drop at all observational levels suggested that the highest level of the tower remained in the interior of the cold pool. Compared to the preceding cold pool of MCS-A, MCS-B generated a deeper and stronger cold pool, when given the magnitude of temperature deficits as cold pool strength. As MCS-B moved away from the tower, the temperature gradually increased after 2156 LST. The temperature recovery near the surface was relatively weak and slow compared to that at higher levels. After the passage of the second cold pool, a stable nocturnal low-level stratification developed.

The shallow cold pool from MCS-A was detected with a smaller temperature deficit and quick distinct temperature recovery at high levels, whereas the deep cold pool from MCS-B caused a more intense temperature deficit and weak recovery afterward at all measurement levels. The evolution of reflectivity at different levels at the Met-Tower position derived from

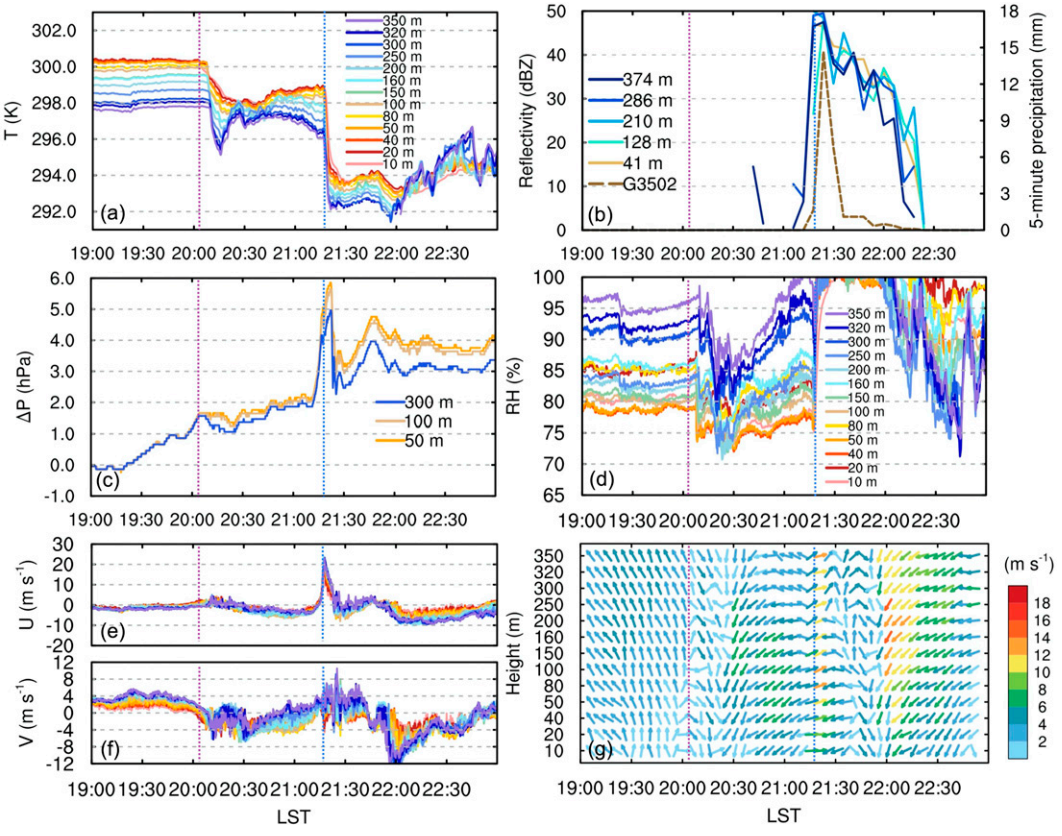

FIG. 6. Time series of (a) temperature (K), (b) reflectivity (dBZ) and 5-min precipitation (mm), (c) pressure perturbation (hPa), (d) relative humidity (%), (e) U component wind (m s^{-1}), (f) V component wind (m s^{-1}), and (g) horizontal wind vectors (m s^{-1}) at different levels at Shenzhen Met-Tower during the heavy rainfall event on 11 Apr 2019. The dashed brown line in (b) represents the evolution of 5-min precipitation at station G3502, and the solid lines show the evolution of radar reflectivity at the tower. Vertical dashed lines in each panel denote the start of cooling at the lowest layer (10 m). The undisturbed state relative to pressure perturbation is the temporal average between 1800 and 1900 LST.

Shenzhen radar data showed that the passage of convective systems only occurred at the second cold pool (2116 LST, Fig. 6b). The results reveal that the shallow density current propagated away from its parent MCS-A, while the deep cold pool passed by Shenzhen Met-Tower was closely accompanied by the convective system (MCS-B).

The pressure increases at all observed levels were accompanied by temperature decreases during the two passages of cold pools (Fig. 6c) due to the arrival of colder and denser air masses based on the hydrostatic relation. Pressure in the shallow cold pool increased 0.7 hPa, while pressure obtained a larger enhancement of 3 hPa by the later deeper cold pool. The increase in pressure occurred 12 min before the temperature decreased and persisted for a short time (e.g., only 14 min in the second process). The earlier onset of pressure increases than temperature reduction was also found in other studies (e.g., Kirsch et al. 2021; Engerer et al. 2008).

After the temperature decreased in the shallow cold pool, the relative humidity decreased 16% at 300 m (Fig. 6d). Then, the relative humidity recovered with the recovering temperature. During the deep cold pool that passed at 2116 LST, the atmosphere first became drier and then reached saturation rapidly because of the intense temperature decrease. To clearly quantify the variations in moisture in the boundary layer, we further calculated the specific humidity using the observed temperature, pressure, and relative humidity (Fig. 7a). Passage of the shallow cold pool resulted in -3.73 g kg^{-1} of specific humidity at 50 m and -4.44 g kg^{-1} at 300 m, while the deep cold pool caused -1.20 g kg^{-1} at 50 m and -2.48 g kg^{-1} at 300 m. Passages of two cold pools dried the boundary layer at all observed levels and dried more strongly at higher layers. It shows no significant moisture enhancement before passages of the two cold pools, and moisture decreased afterward, which indicates a drier interior of cold pools. These variations in moisture do not suggest the existence of a moisture ring structure.

The complicated variations in specific humidity are considered to reflect the interaction of various formation processes of cold pools: 1) evaporation cooling, which can moisten the atmosphere, and 2) vertical import of upper-level dry air masses, which can dry the atmosphere (Kirsch et al. 2021). Kirsch et al. (2021) found that the evaporative cooling process at midlatitudes contributes more to variability in temperature

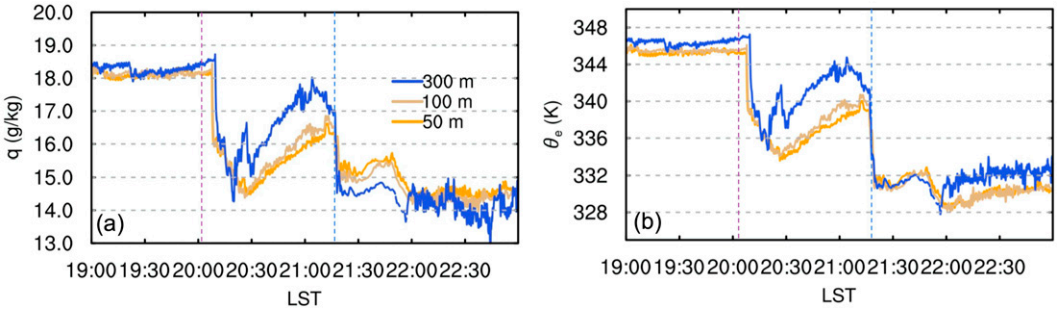

FIG. 7. Time series of (a) calculated specific humidity (q, g kg^{-1}) and (b) equivalent potential temperature (θ_e, K) at three measurement levels of Shenzhen Met-Tower during the heavy rainfall event on 11 Apr 2019. Vertical dashed lines denote the start of cooling at the lowest layer (10 m).

perturbation by cold pools and that the passage of cold pools on average leads to moistening in the boundary layer. However, a decrease in specific humidity is usually observed by cold pool passages in the tropics (e.g., Schiro and Neelin 2018; de Szoeke et al. 2017). In this case, variations in specific humidity during the two cold pools suggest that the influence of rainfall evaporation was weaker than the convective downward import of upper dry air mass in the current case of South China. The import of upper-level dry and cold air masses also caused stronger drying in higher layers. Figure 7b shows the time series of the equivalent potential temperature (θ_e). The decreases in θ_e documented in the two cold pool passages also suggest that the entrainment of cold and dry air from upper altitudes (e.g., midlevels) dominated the changes in specific humidity (Zuidema et al. 2012), which contrasts to cold pools that increased θ_e by precipitation evaporation (e.g., Wood et al. 2011).

Figures 6e–g display the temporal evolution of horizontal winds associated with cold pools. As the gust front ahead of the shallow cold pool approached, the direction of wind gradually veered from background southeasterly winds to northwesterly winds (Fig. 6g). Correspondingly, the V wind component shifted from southerly to northly and the U wind component shifted from easterly to westerly near the appearance of the first temperature deficit (Figs. 6e,f). The acceleration of wind speed was relatively weak during the initial cooling (~2 m s^{-1}, Fig. 6g). After the warm air intrusion at the top of the shallow cold pool where temperature increased significantly above 100 m (Fig. 6a), turbulence appeared at the wake of the cold pool head and was presented as winds at higher levels (above 150 m) frequently switched between northerly and southerly (Figs. 6f,g, e.g., Charba 1974; Simpson 1969). The Met-Tower detected the properties of the head structure at the top of the shallow cold pool, which were observed with two couplets of temperature deficit and rising at higher levels (Fig. 6a) as well as turbulent winds (Fig. 6g).

As the deep cold pool of MCS-B passed, the winds were greatly accelerated by nearly 15 m s^{-1}, presenting as a strong gust front (Fig. 6g). The wind direction was abruptly turned westerly and yielded a significant increase in the U component from a weak easterly to a strong westerly (Figs. 6e,g). The wind shifts by gust fronts agreed with the expected wind direction changes according to the relative positions and movement directions of the corresponding MCSs to the tower (Fig. 2).

Compared with the cold pool observations in another case in coastal South China (Wang et al. 2014), the shallow cold pool in this case caused a weaker surface temperature deficit and a shift in wind direction, whereas the deep cold pool caused a more intense surface temperature deficit signal. Distinct from the temperature deficit, the drying magnitudes of specific humidity by the first cold pool were larger than those in the second cold pool. The smaller drying might be related to the accompanying on-going precipitation, which can reduce the extent of drying through moisture evaporation. Despite a decrease in specific humidity, the deep cold pool generated a saturated boundary layer due to intense cooling.

5. Heavy rainfall associated with colliding cold pools

Strong convective precipitation was produced in Shenzhen by the bowed echo, and long-lasting precipitation occurred in the southern downtown area. During the intense precipitation episode, two cold pools featuring varying characteristics were observed by Shenzhen Met-Tower. The detailed effects of these two cold pools on the production and persistence of heavy rainfall in Shenzhen are further investigated through observations in the following section.

a. Evolution of cold pools and MCSs

To investigate the influences of cold pools, the positions of the two cold pools need to be clarified first. The leading edges of cold pools can be identified as equivalent potential temperature perturbations or temperature depressions reaching a certain threshold (e.g., Schlemmer and Hohenegger 2014, 2016). Here, we identified the position of the cold pool leading edge as where equivalent potential temperature perturbation (θ_e') falls below a threshold of −4 K. The θ_e' in the current study is calculated by the differences between θ_e at that time step calculated from in situ station observations and unperturbed θ_e. The unperturbed θ_e is the average during 1800–1900 LST when Shenzhen Met-Tower had not undergone obvious cooling from cold pools. The leading edges of cold pools are along the contour of −4 K, which is obtained from natural neighbor interpolation of θ_e'.

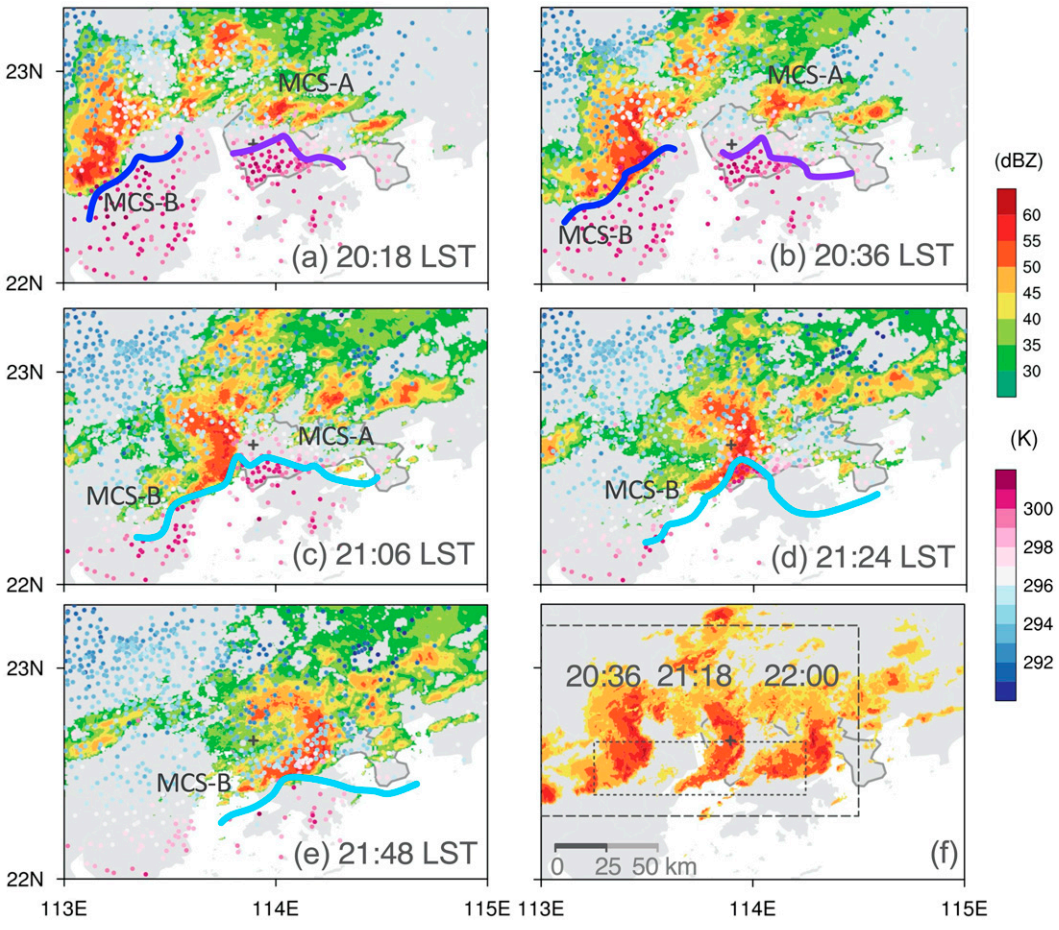

FIG. 8. Temporal evolution of composite reflectivity over 25 dBZ (dBZ, shaded) and surface temperature (K, dots) at (a) 2018, (b) 2036, (c) 2106, (d) 2124, and (e) 2148 LST 11 Apr 2019. The solid lines represent the positions of the cold pool leading edges associated with MCS-A (purple), MCS-B (blue), and the merged cold pools (cyan). The crosses denote the locations of Shenzhen Met-Tower. (f) Composite reflectivity above 40 dBZ (shaded) at 2036, 2118, and 2200 LST to show the morphological evolutions of MCS-B. The dotted and dashed boxes denote the range for average calculation in Figs. 10a and 10b, respectively.

Zoomed in on Fig. 2, Fig. 8 displays the detailed evolution of MCSs and the corresponding movement of cold pools. MCS-A passed north of Shenzhen city and generated a cold pool (its southern leading edge is denoted as purple solid line in Fig. 8a). When MCS-A propagated northeastward under the southwesterly steering flow, the leading edge of its cold pool nearly stagnated (Fig. 8a). The separated cold pool then moved slowly southward to the tower and caused the first temperature deficit at the tower (Fig. 6a).

Originating from the west, MCS-B was organized into a squall line (Figs. 8a–c). MCS-B propagated eastward in close proximity to its cold pool (blue line). At 2106 LST, MSC-B and its strong cold pool, which caused a large temperature deficit, arrived at the Pearl River Estuary. Meanwhile, the strong cold pool by MCS-B collided with the weak cold pool by MCS-A (Fig. 8c). Then, the merged cold pool and MCS-B continued to move eastward together. When the merged cold pool and MCS-B passed through the Met-Tower, it caused a stronger temperature decrease and gusty wind acceleration (Figs. 6a,g). In Fig. 6, the simultaneous appearance of strong gust wind, intense cooling and high radar reflectivity suggests a close distance between MCS-B and its cold pool leading edge. As the bow-shaped echo MCS-B reached Shenzhen city, the northern portion of MCS-B gradually weakened, while its southern portion was sustained and slowly progressed eastward (Figs. 8d,e). In addition, as the southern portion continued to develop eastward, the orientation of MCS-B then shifted from a nearly north–south direction to northeast–southwest direction (Figs. 8e,f).

Figure 9b further presents the propagation of cold pools with a longitude–time Hovmöller diagram derived from in situ surface stations at approximately 22.7°N (Fig. 9a). Since 2000 LST, a notable decrease of ~3 K in temperature had been sustained east of 113.8°E (purple arrow in Fig. 9b), which denotes the lasting cooling by the weak shallow cold pool. Meanwhile, intense cooling propagated eastward with a general movement speed of 16.6 m s^{-1} (blue arrow in Fig. 9b). This cooling corresponded to the existence of the deep cold pool and presented as a strong

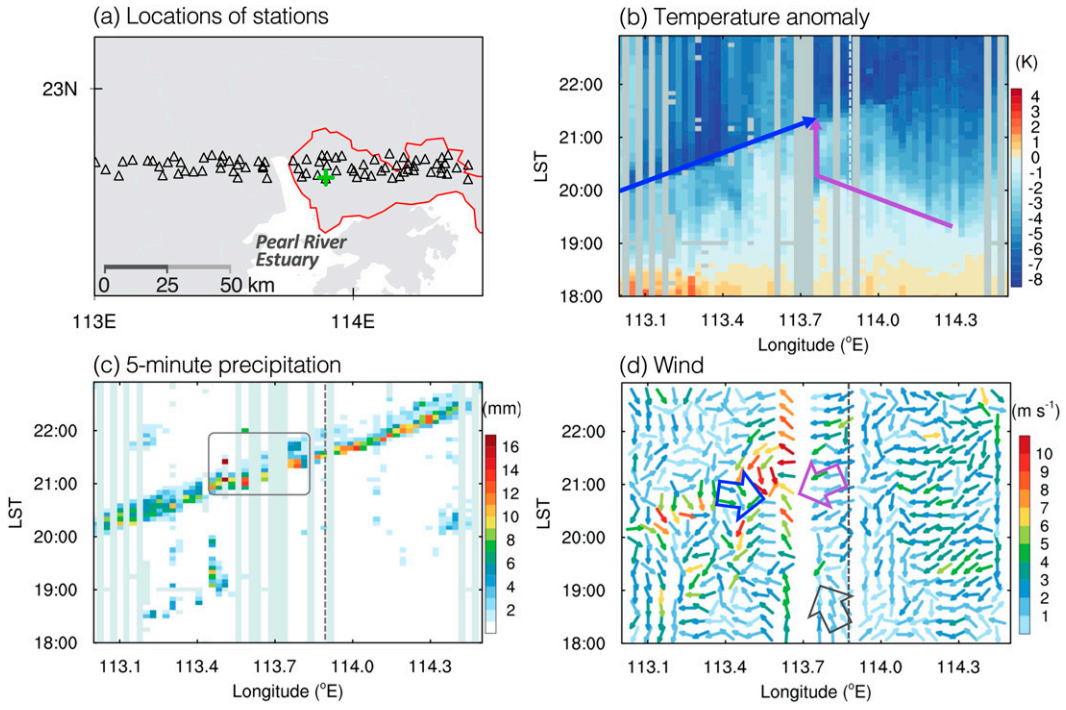

FIG. 9. (a) Locations of in situ surface stations (triangles) near 22.7°N used in (b)–(d). The green cross represents the location of Shenzhen Met-Tower. The red outline represents the range of Shenzhen city. (b)–(d) Longitude–time Hovmöller diagrams of (b) surface temperature anomalies (K), (c) 5-min precipitation (mm), and (d) surface horizontal wind vectors (m s^{-1}) from the stations shown in (a). Vertical dashed lines show the longitude of Shenzhen Met-Tower (113.89°E). The temperature anomaly is the difference relative to the temporal average of 1800–1900 LST. The purple and blue arrows in (b) represent the movement of cold pools from MCS-A and MCS-B, respectively. The square in (c) highlights the strengthening of precipitation. The black and purple arrows in (d) generally indicate the wind direction shift affected by the cold pool from MCS-A, and the blue and purple arrows in (d) roughly show the convergence near the Pearl River Estuary.

boundary (large horizontal gradient) of the temperature anomaly. After 2100 LST, the strong cooling edge encountered and merged with the precedent quasi-stationary weak cold pool near the Pearl River Estuary. As the merged cold pool moved through Shenzhen, the zonal temperature difference between the cold pool and the ambient environment weakened.

b. Precipitation enhancement due to cold pool collision

From the longitude-time Hovmöller diagram of 5-min precipitation in Fig. 9c, precipitation moved eastward synchronously with the eastward strong temperature decrease in Fig. 9b. The rainfall in Shenzhen city was thus mainly produced by MCS-B. Precipitation strengthened near the Pearl River Estuary. In the horizontal wind field, the direction of the southeasterly surface background wind veered after the arrival of the weak cold pool and to northeasterly near 2100 LST (black and purple arrows in Fig. 9d). Changes in wind direction were also observed by Shenzhen Met-Tower, as shown in the previous section, in which the weak gust front shifted winds from background southeasterly to northwesterly and turned to northeasterly near 2030 LST (Figs. 6e–g). In the west, the strong nearly westerly gust front moved eastward with the propagation of the deep cold pool (blue arrow, Figs. 9b–d). Surface winds at the rear of the nearly westerly gust front gradually veered to northeasterly as the convective portion of MCS-B passed by. When the intense gust front moved to the Pearl River Estuary, its intense nearly westerly could strongly converge with the northeasterly that was previously influenced by the weak gust front (blue and purple arrows in Fig. 9d) and dynamically enhance the precipitation near the Pearl River Estuary (Fig. 9c). The enhanced rainfall later maintained and moved eastward, finally bringing heavy rainfall to Shenzhen (Fig. 9c).

Figures 8 and 9b both show the collision between the two cold pools. As in many previous studies, collision between mesoscale boundaries is a trigger for new convection and a maintenance mechanism for MCSs (e.g., Droegemeier and Wilhelmson 1985a, b; Torri et al. 2015; Feng et al. 2015; Purdom 1976; Torri and Kuang 2019). The collision of cold pools can help the interaction of positive pressure anomalies at their leading edges, generating strong vertical motion to lift air parcels. When the gust front of the merged cold pool passed by Shenzhen, the strong wind gusts caused by convective downdrafts weakened. According to the density current theory, the weakened gust front was possibly contributed by the decreased temperature difference and density difference between the cold pool and the environment cooled by the precedent cold pool (Figs. 9b,d, Simpson 1969).

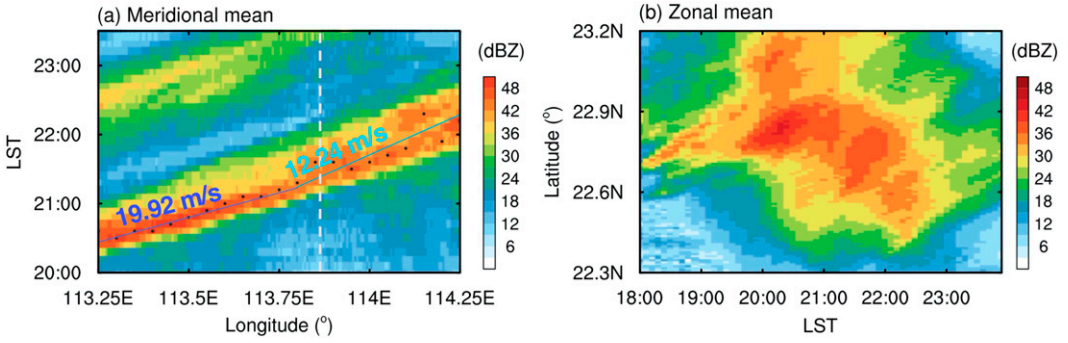

FIG. 10. (a) Longitude–time Hovmöller diagram of composite reflectivity (dBZ) averaged over 22.4°–22.65°N. The vertical dashed line represents the longitude of Shenzhen Met-Tower (113.89°E). The blue and cyan lines show the estimated propagation of the southern part of MCS-B. Black dots are the locations of the maximum composite reflectivity at the longitude. (b) Time–latitude Hovmöller diagram of composite reflectivity (dBZ) averaged over 113°–114.5°E.

c. *Morphological transformation of the MCS due to cold pool collision*

In addition to the enhanced precipitation intensity near Shenzhen city, the large accumulation of rainfall at the southern downtown of Shenzhen was also contributed by the long rainfall duration (Fig. 3).

The long-lasting rainfall was associated with the shift of MCS-B's orientation shown in Fig. 8 and MCS-B's orientation is also shown intuitively in Fig. 8f. The evolution of MCS-B, which mainly produced heavy rainfall in Shenzhen, was further examined with longitude-time or time-latitude Hovmöller diagrams, as shown in Fig. 10. In the west, the convective part (>25 dBZ) in a southern portion of MCS-B (average between 22.4° and 22.65°N, denoted as a dotted box in Fig. 8f) propagated eastward with a similar speed as the cold pool of approximately 19.92 m s^{-1} (Figs. 10a and 9b). The propagation speed was objectively estimated with the linear trend of the maximum composite reflectivity at each longitude in Fig. 10a. There is a difference between the two measured speeds in Fig. 9 and 10a because Fig. 10a focuses on the speed of a portion of MCS-B rather than the whole convective system, and different average areas are adopted in Figs. 9b and 10a. As it reached Shenzhen (east of 113.8°E), the strongly convective portion of the convection extended a considerable distance behind the line. Additionally, the southern part of MCS-B experienced a slight reduction in speed (from 19.92 to 12.24 m s^{-1}). The two factors above result in heavy rainfall passing through a certain longitude over a longer period of time. As shown in Fig. 10b, the northern portion of the bow-echo MCS-B gradually dissipated after 2100 LST when it arrived Shenzhen. The southern portion of MCS-B developed and propagated to the south. MCS-B became shorter in the meridional range. Taken together, MCS-B experienced a shift in its orientation after reaching Shenzhen, from oriented nearly meridionally to zonally, and a slower eastward propagation across southern Shenzhen.

The large cumulative rainfall results from a strong precipitation rate as well as a long duration of rainfall over the same area (Doswell et al. 1996). A large number of extreme rainfall events are contributed by MCSs featuring quasi-stationary or repeated passages of convective cells, which prolongs the duration of rainfall over a particular region (Peters and Schumacher 2015, 2016; Wang et al. 2014; Jeong et al. 2016). As the eastward MCS-B turned northeast–southwest oriented, it was organized into the "training line" mode, which moved nearly parallel to the convective line (Schumacher and Johnson 2005, 2006; Peters and Schumacher 2015). Therefore, MCS-B prolonged the passage time over southern Shenzhen by approximately 50 min, causing heavy rainfall at the most populated downtown (Fig. 3).

It is known from the observations of the tower and surface stations that the weak cold pool cooled the surface of Shenzhen before the arrival of MCS-B, and the low near-surface temperature was sustained for time under stratiform precipitation and nocturnal radiation cooling (Figs. 6a and 9b). When the eastward MCS-B and its cold pool arrived at Shenzhen, the deep cold pool collided with the weak cold pool. As MCS-B and the merged cold pool further propagated into Shenzhen, the leading edge of the merged cold pool did not coincide well with the bow-shaped echo as it did previously (Figs. 8a–c). Before collision with the shallow cold pool, large temperature gradients perpendicular to the edge of MCS-B were both at the northern (0.34 K km^{-1}) and southern edges (0.6 K km^{-1}). The shallow cool pool cooled the ambient temperature at Shenzhen and reduced the temperature difference with the merged cold pool interior, so the edge of the merged cold pool was away from the north end of MCS-B. The temperature gradient in the northern portion of MCS-B was thus small (approximately 0.15 K km^{-1}, Fig. 8c), which can also be seen from Fig. 9b. Then, near the edge of the northern portion of MCS-B, the gust front and the associated lifting were likely weak; additionally, few new convective cells could be initiated there. Under the lower possibility of convection initiation, the northern portion of the bow-shaped echo MCS-B would gradually dissipate (Figs. 8 and 10b).

For the southern portion of the bow-shaped echo, the ambient surface temperature in southern Shenzhen was unaffected by the precedent shallow cold pool. The ambient surface temperature was much higher due to the southwesterly warm-moist flow (Figs. 8c–e). In addition to the surface temperature

decrease in the interior of the deep cold pool, the temperature inside the cold pool was much lower than the exterior ambient temperature. Therefore, there was still a large temperature gradient (approximately 0.6 K km^{-1}) along the south edge of the cold pool. The temperature gradient is relevant to the buoyancy gradient. The horizontal buoyancy gradient can baroclinically generate horizontal vorticity and provide upward motions (e.g., Trapp and Weisman 2003; Wu and Lombardo 2021). Warm and moist air through the low-level southwesterly from the ocean can then be lifted. Thus, the large temperature gradient along the cold pool edge was beneficial to the gust front and updrafts initiating convections and maintaining MCS. The southern portion of the bow-shaped echo could continue developing and sustain. MCS-B also tended to move southeastward under the favorable conditions at the southern edge. Combining the dissipation of the north end and the slow eastward movement of the south portion, MCS-B evolved from north–south oriented to northeast–southwest oriented under the changes in horizontal thermodynamic distribution by the cold pools colliding. Finally, MCS-B turned to a training line mode and achieved a longer residency over the southern downtown for approximately 50 min, resulting in large losses in the area.

6. Summary and discussion

Convectively driven cold pools are an important factor for convection initiation and MCS development, but their quantitative observational features in South China have been seldom studied, which limits our ability to accurately represent cold pools and the associated precipitation in numerical models for this region. On 11 April 2019, an extremely heavy rainfall event produced a maximum 30-min rainfall of 73.4 mm over Shenzhen city, resulting in significant losses. The present study applies Shenzhen Met-Tower data to examine the vertical structure of cold pools in this event and to provide an observational reference dataset for cold pool evolution. The study also investigates the potential influences of cold pools on the heavy rainfall at Shenzhen in conjunction with radar and surface in situ station observations.

Observations from the Shenzhen Met-Tower show the passages of two cold pools with different intensities. The first shallow cold pool yielded a cooling of 2.6 K at all measurement layers. The head structure of the shallow cold pool was observed above 100 m with evident temperature fluctuations and wind turbulence, which suggests an estimation cold pool body depth of approximately 100 m. The second deep cold pool caused a stronger temperature drop of 5.1 K at 10 m 1 h later. The temperature drop decreased in higher layers (4 K at 300 m). Pressure increases were observed nearly 12 min prior to cooling. Similar magnitudes of pressure increase occurred in all layers: 0.7 hPa in the shallow cold pool and 3 hPa in the deep cold pool. The cold pool passages resulted in a change in the horizontal wind direction, with the shallow cold pool leading to weak wind acceleration (~2 m s^{-1}) and the deep cold pool causing intense gust wind acceleration of more than 15 m s^{-1}. No significant moisture enhancement occurred ahead of the cold pool, suggesting the absence of a moisture ring. The interior of the cold pool became drier, similar to a cold pool study over the Netherlands (Kruse et al. 2022). The shallow cold pool dried the atmosphere strongly for −3.73 g kg^{-1} of specific humidity at 50 m and was drier at higher levels (−4.44 g kg^{-1} of specific humidity at 300 m). The observed variations in moisture with height are in contrast to those reported in Germany by Kirsch et al. (2021), where enhanced moisture occurs in the cold pool interior and moister at higher levels. These differences in vertical structures may suggest variations in the contributions of rainfall evaporation and vertical transport of upper-level air masses in these regions. Although the deep cold pool yielded larger signals of temperature, pressure and horizontal wind speed, the drying effect was relatively weak (−1.20 g kg^{-1} of specific humidity at 50 m and −2.48 g kg^{-1} at 300 m), which may be relevant to the simultaneous arrival of rainfall evaporation. The stronger cooling of the deeper cold pool led to the formation of a saturated boundary layer.

In this case, precipitation was intensified near Shenzhen and lasted longer in the southern downtown area of Shenzhen due to the collision of two cold pools. Figure 11 provides schematic diagrams illustrating the potential effects of this colliding on the strengthening of precipitation and the transformation of the morphology of MCS. Low-level winds converged at the gust fronts of the two cold pools, dynamically intensifying precipitation near the Pearl River Estuary (Fig. 11a). As MCS-B moved farther east with the merged cold pool, it transformed into a training line–type MCS, with a morphology parallel to its movement direction (Fig. 11b). Previous case studies (e.g., Peters and Schumacher 2015, 2016; Wang et al. 2014; Liu et al. 2018) have documented that back-building or training MCSs usually form as unstable air parcels with high CAPE are lifted by isentropic upglide and baroclinicity associated with the cold pool caused by a forward-propagating MCS, initiating and developing convection upstream of the MCS. Similarly, in this case, the warm ambient environment from the ocean retained a large temperature gradient and generated baroclinicity at the southern edge of MCS-B, promoting convection triggering and maintenance. On the other hand, detailed observations of the evolution of the cold pools indicate that surface cooling by the precedent shallow cold pool reduced the temperature gradient at the northern leading edge of the subsequent deep cold pool. As a result, after the cold pool collision, the weak temperature difference at the front of the merged cold pool decreased the likelihood of isentropic upglide and unfavored the northern portion of MCS-B maintenance. In addition to intense mechanical lifting produced by cold pool collision (Feng et al. 2015; Haerter 2019; Torri and Kuang 2019; Meyer and Haerter 2020), the collision also altered the horizontal thermodynamic distribution, which contributed to a transition in MCS-B's organizational structure. The transformed training line MCS-B crossed southern Shenzhen with a new northeast–southwest orientation, resulting in longer residency of heavy rainfall in the densely populated downtown area.

The present study investigates the processes and mechanisms of cold pools purely from an observational perspective. The findings suggest that colliding cold pools may potentially strengthen precipitation and transform the morphology of

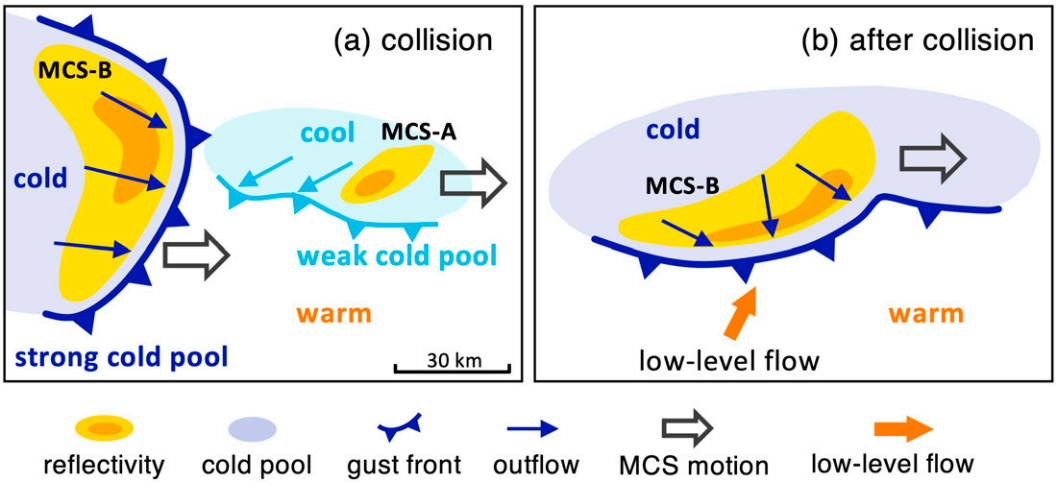

FIG. 11. Schematic diagrams of the effects of colliding cold pools on strengthening precipitation or transforming the morphology of MCS in this heavy rainfall event (a) during the collision process and (b) after the collision. Shading in yellow and orange roughly represents radar reflectivity of 45 and 55 dB*Z*.

heavy-rainfall-producing MCS. However, other factors, such as the southwest–northeast-oriented coastline and coastal terrain (Du et al. 2020a,b, 2022), where the marine boundary layer jets converge and provide lifting for convection triggering due to land-sea differential friction and topographic mechanical lifting, may also influence the enhancement and change in orientation of MCS-B. Investigating their relative contributions and detailed mechanisms of these factors requires numerical simulations and related sensitivity experiments. Moreover, the dataset derived from the Shenzhen Met-Tower has high temporal and vertical resolutions, making it an essential observational reference for comparison against high-resolution simulations in South China, which can help improve the ability to accurately represent precipitation (Kirsch et al. 2021; Rio et al. 2009). To establish a reference dataset with higher reliability and compare it with other regions (e.g., Engerer et al. 2008; de Szoeke et al. 2017; Joseph et al. 2021), further examination of the magnitude and vertical variations of perturbations caused by cold pools in the boundary layer is necessary for climatology near the coastal South China region.

Acknowledgments. This study was supported by the Guangdong Major Project of Basic and Applied Basic Research (2020B0301030004), the National Natural Science Foundation of China (Grants 42122033, 42075006, and U21A6001).

Data availability statement. The observational data of radar, in situ surface stations, and radiosonde soundings were obtained from the National Meteorological Information Center of the China Meteorological Administration, and available at http://data.cma.cn. The NCEP FNL reanalysis data from NCAR are available at https://rda.ucar.edu/datasets/ds083.3/. The equivalent potential temperature is calculated with the function in NCL (https://www.ncl.ucar.edu/Document/Functions/Contributed/pot_temp_equiv.shtml).

REFERENCES

Alduchov, O. A., and R. E. Eskridge, 1996: Improved Magnus form approximation of saturation vapor pressure. *J. Appl. Meteor. Climatol.*, **35**, 601–609, https://doi.org/10.1175/1520-0450(1996)035<0601:IMFAOS>2.0.CO;2.

Borque, P., S. W. Nesbitt, R. J. Trapp, S. Lasher-Trapp, and M. Oue, 2020: Observational study of the thermodynamics and morphological characteristics of a midlatitude continental cold pool event. *Mon. Wea. Rev.*, **148**, 719–737, https://doi.org/10.1175/MWR-D-19-0068.1.

Bryan, G. H., and R. Rotunno, 2014: The optimal state for gravity currents in shear. *J. Atmos. Sci.*, **71**, 448–468, https://doi.org/10.1175/JAS-D-13-0156.1.

Chandra, A. S., P. Zuidema, S. Krueger, A. Kochanski, S. P. de Szoeke, and J. Zhang, 2018: Moisture distributions in tropical cold pools from equatorial Indian Ocean observations and cloud-resolving simulations. *J. Geophys. Res. Atmos.*, **123**, 11 445–11 465, https://doi.org/10.1029/2018JD028634.

Charba, J., 1974: Application of gravity current model to analysis of squall-line gust front. *Mon. Wea. Rev.*, **102**, 140–156, https://doi.org/10.1175/1520-0493(1974)102<0140:AOGCMT>2.0.CO;2.

Chen, B., J. Yang, R. Gao, K. Zhu, C. Zou, Y. Gong, and R. Zhang, 2020: Vertical variability of the raindrop size distribution in typhoons observed at the Shenzhen 356-m meteorological tower. *J. Atmos. Sci.*, **77**, 4171–4187, https://doi.org/10.1175/JAS-D-20-0043.1.

Chen, Y., Y. Luo, and B. Liu, 2022: General features and synoptic-scale environments of mesoscale convective systems over South China during the 2013–2017 pre-summer rainy seasons. *Atmos. Res.*, **266**, 105954, https://doi.org/10.1016/j.atmosres.2021.105954.

Del Genio, A. D., Y. Chen, D. Kim, and M.-S. Yao, 2012: The MJO transition from shallow to deep convection in *CloudSat/CALIPSO* data and GISS GCM simulations. *J. Climate*, **25**, 3755–3770, https://doi.org/10.1175/JCLI-D-11-00384.1.

de Szoeke, S. P., E. D. Skyllingstad, P. Zuidema, and A. S. Chandra, 2017: Cold pools and their influence on the tropical marine boundary layer. *J. Atmos. Sci.*, **74**, 1149–1168, https://doi.org/10.1175/JAS-D-16-0264.1.

Doswell, C. A., III, H. E. Brooks, and R. A. Maddox, 1996: Flash flood forecasting: An ingredients-based methodology. *Wea. Forecasting*, **11**, 560–581, https://doi.org/10.1175/1520-0434(1996)011<0560:FFFAIB>2.0.CO;2.

Droegemeier, K. K., and R. B. Wilhelmson, 1985a: Three-dimensional numerical modeling of convection produced by interacting thunderstorm outflows. Part I: Control simulation and low-level moisture variations. *J. Atmos. Sci.*, **42**, 2381–2403, https://doi.org/10.1175/1520-0469(1985)042<2381:TDNMOC>2.0.CO;2.

——, and ——, 1985b: Three-dimensional numerical modeling of convection produced by interacting thunderstorm outflows. Part II: Variations in vertical wind shear. *J. Atmos. Sci.*, **42**, 2404–2414, https://doi.org/10.1175/1520-0469(1985)042<2404:TDNMOC>2.0.CO;2.

Du, Y., G. Chen, B. Han, C. Mai, L. Bai, and M. Li, 2020a: Convection initiation and growth at the coast of South China. Part I: Effect of the marine boundary layer jet. *Mon. Wea. Rev.*, **148**, 3847–3869, https://doi.org/10.1175/MWR-D-20-0089.1.

——, ——, ——, L. Bai, and M. Li, 2020b: Convection initiation and growth at the coast of South China. Part II: Effects of the terrain, coastline, and cold pools. *Mon. Wea. Rev.*, **148**, 3871–3892, https://doi.org/10.1175/MWR-D-20-0090.1.

——, Y. Shen, and G. Chen, 2022: Influence of coastal marine boundary layer jets on rainfall in South China. *Adv. Atmos. Sci.*, **39**, 782–801, https://doi.org/10.1007/s00376-021-1195-7.

Engerer, N. A., D. J. Stensrud, and M. C. Coniglio, 2008: Surface characteristics of observed cold pools. *Mon. Wea. Rev.*, **136**, 4839–4849, https://doi.org/10.1175/2008MWR2528.1.

Feng, Z., S. Hagos, A. K. Rowe, C. D. Burleyson, M. N. Martini, and S. P. de Szoeke, 2015: Mechanisms of convective cloud organization by cold pools over tropical warm ocean during the AMIE/DYNAMO field campaign. *J. Adv. Model. Earth Syst.*, **7**, 357–381, https://doi.org/10.1002/2014MS000384.

Geerts, B., and Coauthors, 2017: The 2015 Plains Elevated Convection at Night Field Project. *Bull. Amer. Meteor. Soc.*, **98**, 767–786, https://doi.org/10.1175/BAMS-D-15-00257.1.

Grant, L. D., and S. C. van den Heever, 2016: Cold pool dissipation. *J. Geophys. Res. Atmos.*, **121**, 1138–1155, https://doi.org/10.1002/2015JD023813.

Goff, R. C., 1976: Vertical structure of thunderstorm outflows. *Mon. Wea. Rev.*, **104**, 1429–1440, https://doi.org/10.1175/1520-0493(1976)104<1429:VSOTO>2.0.CO;2.

Haerter, J. O., 2019: Convective self-aggregation as a cold pool-driven critical phenomenon. *Geophys. Res. Lett.*, **46**, 4017–4028, https://doi.org/10.1029/2018GL081817.

Hirt, M., and G. C. Craig, 2021: A cold pool perturbation scheme to improve convective initiation in convection-permitting models. *Quart. J. Roy. Meteor. Soc.*, **147**, 2429–2447, https://doi.org/10.1002/qj.4032.

Hitchcock, S. M., R. S. Schumacher, G. R. Herman, M. C. Coniglio, M. D. Parker, and C. L. Ziegler, 2019: Evolution of pre- and postconvective environmental profiles from mesoscale convective systems during PECAN. *Mon. Wea. Rev.*, **147**, 2329–2354, https://doi.org/10.1175/MWR-D-18-0231.1.

Jeong, J.-H., D.-I. Lee, and C.-C. Wang, 2016: Impact of the cold pool on mesoscale convective system–produced extreme rainfall over southeastern South Korea: 7 July 2009. *Mon. Wea. Rev.*, **144**, 3985–4006, https://doi.org/10.1175/MWR-D-16-0131.1.

Joseph, J., M. S. Girishkumar, M. J. McPhaden, and E. Pattabhi Rama Rao, 2021: Diurnal variability of atmospheric cold pool events and associated air-sea interactions in the Bay of Bengal during the summer monsoon. *Climate Dyn.*, **56**, 837–853, https://doi.org/10.1007/s00382-020-05506-w.

Kirsch, B., F. Ament, and C. Hohenegger, 2021: Convective cold pools in long-term boundary layer mast observations. *Mon. Wea. Rev.*, **149**, 811–820, https://doi.org/10.1175/MWR-D-20-0197.1.

Kruse, I. L., J. O. Haerter, and B. Meyer, 2022: Cold pools over the Netherlands: A statistical study from tower and radar observations. *Quart. J. Roy. Meteor. Soc.*, **148**, 711–726, https://doi.org/10.1002/qj.4223.

Li, L., and Coauthors, 2020: Tower observed vertical distribution of $PM_{2.5}$, O_3 and NO_x in the Pearl River Delta. *Atmos. Environ.*, **220**, 117083, https://doi.org/10.1016/j.atmosenv.2019.117083.

Liu, X., Y. Luo, Z. Guan, and D.-L. Zhang, 2018: An extreme rainfall event in coastal South China during SCMREX-2014: Formation and roles of rainband and echo trainings. *J. Geophys. Res. Atmos.*, **123**, 9256–9278, https://doi.org/10.1029/2018JD028418.

Luo, L., M. Xue, and K. Zhu, 2020: The initiation and organization of a severe hail-producing mesoscale convective system in East China: A numerical study. *J. Geophys. Res. Atmos.*, **125**, e2020JD032606, https://doi.org/10.1029/2020JD032606.

Maddox, R. A., C. F. Chappell, and L. R. Hoxit, 1979: Synoptic and meso-α scale aspects of flash flood events. *Bull. Amer. Meteor. Soc.*, **60**, 115–123, https://doi.org/10.1175/1520-0477-60.2.115.

Maloney, E. D., and D. L. Hartmann, 2001: The sensitivity of intraseasonal variability in the NCAR CCM3 to changes in convective parameterization. *J. Climate*, **14**, 2015–2034, https://doi.org/10.1175/1520-0442(2001)014<2015:TSOIVI>2.0.CO;2.

Meyer, B., and J. O. Haerter, 2020: Mechanical forcing of convection by cold pools: Collisions and energy scaling. *J. Adv. Model. Earth Syst.*, **12**, e2020MS002281, https://doi.org/10.1029/2020MS002281.

Miller, R. L., C. L. Ziegler, and M. I. Biggerstaff, 2020: Seven-Doppler radar and in situ analysis of the 25–26 June 2015 Kansas MCS during PECAN. *Mon. Wea. Rev.*, **148**, 211–240, https://doi.org/10.1175/MWR-D-19-0151.1.

Peters, J. M., and R. S. Schumacher, 2015: Mechanisms for organization and echo training in a flash-flood-producing mesoscale convective system. *Mon. Wea. Rev.*, **143**, 1058–1085, https://doi.org/10.1175/MWR-D-14-00070.1.

——, and ——, 2016: Dynamics governing a simulated mesoscale convective system with a training convective line. *J. Atmos. Sci.*, **73**, 2643–2664, https://doi.org/10.1175/JAS-D-15-0199.1.

Purdom, J. F. W., 1976: Some uses of high-resolution GOES imagery in the mesoscale forecasting of convection and its behavior. *Mon. Wea. Rev.*, **104**, 1474–1483, https://doi.org/10.1175/1520-0493(1976)104<1474:SUOHRG>2.0.CO;2.

Rio, C., F. Hourdin, J.-Y. Grandpeix, and J.-P. Lafore, 2009: Shifting the diurnal cycle of parameterized deep convection over land. *Geophys. Res. Lett.*, **36**, L07809, https://doi.org/10.1029/2008GL036779.

Rotunno, R., J. B. Klemp, and M. L. Weisman, 1988: A theory for strong, long-lived squall lines. *J. Atmos. Sci.*, **45**, 463–485, https://doi.org/10.1175/1520-0469(1988)045<0463:ATFSLL>2.0.CO;2.

Schiro, K. A., and J. D. Neelin, 2018: Tropical continental downdraft characteristics: Mesoscale systems versus unorganized convection. *Atmos. Chem. Phys.*, **18**, 1997–2010, https://doi.org/10.5194/acp-18-1997-2018.

Schlemmer, L., and C. Hohenegger, 2014: The formation of wider and deeper clouds as a result of cold-pool dynamics. *J. Atmos. Sci.*, **71**, 2842–2858, https://doi.org/10.1175/JAS-D-13-0170.1.

——, and ——, 2016: Modifications of the atmospheric moisture field as a result of cold-pool dynamics. *Quart. J. Roy. Meteor. Soc.*, **142**, 30–42, https://doi.org/10.1002/qj.2625.

Schumacher, R. S., and R. H. Johnson, 2005: Organization and environmental properties of extreme-rain-producing mesoscale convective systems. *Mon. Wea. Rev.*, **133**, 961–976, https://doi.org/10.1175/MWR2899.1.

——, and ——, 2006: Characteristics of U.S. extreme rain events during 1999–2003. *Wea. Forecasting*, **21**, 69–85, https://doi.org/10.1175/WAF900.1.

Simpson, J. E., 1969: A comparison between laboratory and atmospheric density currents. *Quart. J. Roy. Meteor. Soc.*, **95**, 758–765, https://doi.org/10.1002/qj.49709540609.

Sun, T., and Coauthors, 2020: Time-resolved black carbon aerosol vertical distribution measurements using a 356-m meteorological tower in Shenzhen. *Theor. Appl. Climatol.*, **140**, 1263–1276, https://doi.org/10.1007/s00704-020-03168-6.

Sun, X., Y. Luo, X. Gao, M. Wu, M. Li, L. Huang, D.-L. Zhang, and H. Xu, 2021: On the localized extreme rainfall over the Great Bay area in South China with complex topography and strong UHI effects. *Mon. Wea. Rev.*, **149**, 2777–2801, https://doi.org/10.1175/MWR-D-21-0004.1.

Terai, C. R., and R. Wood, 2013: Aircraft observations of cold pools under marine stratocumulus. *Atmos. Chem. Phys.*, **13**, 9899–9914, https://doi.org/10.5194/acp-13-9899-2013.

Tompkins, A. M., 2001: Organization of tropical convection in low vertical wind shears: The role of water vapor. *J. Atmos. Sci.*, **58**, 529–545, https://doi.org/10.1175/1520-0469(2001)058<0529:OOTCIL>2.0.CO;2.

Torri, G., and Z. Kuang, 2016: Rain evaporation and moist patches in tropical boundary layers. *Geophys. Res. Lett.*, **43**, 9895–9902, https://doi.org/10.1002/2016GL070893.

——, and ——, 2019: On cold pool collisions in tropical boundary layers. *Geophys. Res. Lett.*, **46**, 399–407, https://doi.org/10.1029/2018GL080501.

——, ——, and Y. Tian, 2015: Mechanisms for convection triggering by cold pools. *Geophys. Res. Lett.*, **42**, 1943–1950, https://doi.org/10.1002/2015GL063227.

Trapp, R. J., and M. L. Weisman, 2003: Low-level mesovortices within squall lines and bow echoes. Part II: Their genesis and implications. *Mon. Wea. Rev.*, **131**, 2804–2823, https://doi.org/10.1175/1520-0493(2003)131<2804:LMWSLA>2.0.CO;2.

Tsuguti, H., and T. Kato, 2014: Contributing factors of the heavy rainfall event at Amami-Oshima Island, Japan, on 20 October 2010. *J. Meteor. Soc. Japan*, **92**, 163–183, https://doi.org/10.2151/jmsj.2014-202.

van den Heever, S. C., and Coauthors, 2021: The Colorado State University convective CLoud Outflows and UpDrafts Experiment (C3LOUD-Ex). *Bull. Amer. Meteor. Soc.*, **102**, E1283–E1305, https://doi.org/10.1175/BAMS-D-19-0013.1.

Wang, H., Y. Luo, and B. J.-D. Jou, 2014: Initiation, maintenance, and properties of convection in an extreme rainfall event during SCMREX: Observational analysis. *J. Geophys. Res. Atmos.*, **119**, 13 206–13 232, https://doi.org/10.1002/2014JD022339.

Weaver, J. F., and S. P. Nelson, 1982: Multiscale aspects of thunderstorm gust fronts and their effects on subsequent storm development. *Mon. Wea. Rev.*, **110**, 707–718, https://doi.org/10.1175/1520-0493(1982)110<0707:MAOTGF>2.0.CO;2.

Weisman, M. L., and R. Rotunno, 2004: "A theory for strong long-lived squall lines" revisited. *J. Atmos. Sci.*, **61**, 361–382, https://doi.org/10.1175/1520-0469(2004)061<0361:ATFSLS>2.0.CO;2.

——, J. B. Klemp, and R. Rotunno, 1988: Structure and evolution of numerically simulated squall lines. *J. Atmos. Sci.*, **45**, 1990–2013, https://doi.org/10.1175/1520-0469(1988)045<1990:SAEONS>2.0.CO;2.

Wills, S. M., M. F. Cronin, and D. Zhang, 2021: Cold pools observed by uncrewed surface vehicles in the central and eastern tropical Pacific. *Geophys. Res. Lett.*, **48**, e2021GL093373, https://doi.org/10.1029/2021GL093373.

Wood, R., C. S. Bretherton, D. Leon, A. D. Clarke, P. Zuidema, G. Allen, and H. Coe, 2011: An aircraft case study of the spatial transition from closed to open mesoscale cellular convection over the southeast Pacific. *Atmos. Chem. Phys.*, **11**, 2341–2370, https://doi.org/10.5194/acp-11-2341-2011.

Wu, F., and K. Lombardo, 2021: Precipitation enhancement in squall lines moving over mountainous coastal regions. *J. Atmos. Sci.*, **78**, 3089–3113, https://doi.org/10.1175/JAS-D-20-0222.1.

Wu, M., and Y. Luo, 2016: Mesoscale observational analysis of lifting mechanism of a warm-sector convective system producing the maximal daily precipitation in China mainland during pre-summer rainy season of 2015. *J. Meteor. Res.*, **30**, 719–736, https://doi.org/10.1007/s13351-016-6089-8.

Zipser, E. J., 1977: Mesoscale and convective-scale downdrafts as distinct components of squall-line structure. *Mon. Wea. Rev.*, **105**, 1568–1589, https://doi.org/10.1175/1520-0493(1977)105<1568:MACDAD>2.0.CO;2.

Zuidema, P., and Coauthors, 2012: On trade wind cumulus cold pools. *J. Atmos. Sci.*, **69**, 258–280, https://doi.org/10.1175/JAS-D-11-0143.1.

——, G. Torri, C. Muller, and A. Chandra, 2017: A survey of precipitation-induced atmospheric cold pools over oceans and their interactions with the larger-scale environment. *Surv. Geophys.*, **38**, 1283–1305, https://doi.org/10.1007/s10712-017-9447-x.